PCCP

ROYAL SOCIETY OF CHEMISTRY

PAPER

View Article Online
View Journal

Published on 11 December 2019. Downloaded by Universidade Presbiteriana Mackenzie on 12/20/2019 5:36:45 PM.

Check for updates

Cite this: DOI: 10.1039/c9cp06422b

Understanding the unorthodox stabilization of liquid phase exfoliated molybdenum disulfide (MoS_2) in water medium†

Camila L. C. Rodriguez,[a] Pablo A. R. Muñoz,[a] Katarzyna Z. Donato,[ab] Leandro Seixas,[a] Ricardo K. Donato *[ab] and Guilhermino J. M. Fechine*[a]

Received 27th November 2019,
Accepted 11th December 2019

DOI: 10.1039/c9cp06422b

rsc.li/pccp

Molybdenum disulfide is a highly esteemed 2D material with interesting applications in nanoelectronics, composites, biotechnology and beyond. Its production through liquid-phase exfoliation in H_2O is low-cost and eco-friendly. Herein, we present a detailed experimental and theoretical investigation seeking to explain the peculiar stability of MoS_2 in H_2O medium. By combining different microscopic (SEM, AFM and OM), spectrometric (Raman, UV-vis and AFM-FTIR), scattering (DLS) and *ab initio* simulation techniques, an edge-functionalization hypothesis for the excellent solvent properties of water for producing few-layer MoS_2 has been demonstrated.

Introduction

Most of the nanotechnology related areas, in both academia and industry, are eager to find new large scale processes for obtaining two-dimensional (2D) materials since isolating graphene was proven feasible.[1] Among those 2D materials, an emerging class, namely, transition metal dichalcogenides (TMDs), which includes MoS_2, $MoSe_2$, WS_2, $NiTe_2$, *etc.*,[2,3] is a potential game changer in applications such as batteries, membranes, supercapacitors, sensors, catalytic supports and polymer matrix reinforcing fillers.[4–6] In their pristine (bulk) state, these TMD crystals present a lamellar structure similar to graphite,[7] and as graphene they also present singular properties in their 2D monocrystalline structures. One of the most widely studied TMDs is molybdenum disulfide (MoS_2), especially due to its interesting electronic and optical properties.[8] MoS_2 is a semiconductor, presenting an indirect transition (1.29 eV) and a direct gap (1.9 eV) when changed from a bulk crystal into a few-layer 2D crystal.[9] This change results in a huge increase in photoluminescence, making MoS_2 an excellent candidate for several optoelectronic applications.[10,11] MoS_2 monolayers also present excellent mechanical properties (stress at break: ~23 GPa and Young's modulus: ~300 GPa);[12] thus, it is very promising for polymer nanocomposite production.

A MoS_2 monolayer is constituted of two hexagonal planes of sulfur atoms (S) and an intermediate hexagonal plane of molybdenum atoms (Mo), coordinated through ionocovalent interactions in a prismatic trigonal arrangement (S–Mo–S), and associated with other layers through van der Waals interactions.[9,13] These types of interactions ease the layer separation process through different exfoliation methods. For the liquid phase exfoliation (LPE) method specifically, it is important to understand the chemical interactions that occur between solvent and 2D crystal (surface tension). Usually, the solvent's surface tension must match the crystal's surface energy, allowing stronger interaction between them to reach an effective exfoliation process.[14,15] However, the process is not ruled only by surface tension but also by specific interactions with the solvent at the material's edges.[3] Moreover, the solvent's role should not be limited to promoting 2D materials' exfoliation but should also extend to conserving their original crystalline structure and bestowing long-term stabilization.[15]

Considering most of the prediction models, a good MoS_2 solvent should be at least partially hydrophobic, as it presents a surface energy of 44.5 mJ m^{-2} and a water contact angle of 91.6° giving it a hydrophobic character.[16] Nevertheless, the successful MoS_2 LPE and stabilization in H_2O medium, without the use of any stabilizing agent or surfactant, has been recurrently reported in the literature. Common features were observed among these reports, such as the small lateral size of MoS_2 (below 300 nm) and zeta potential around −32 mV.[17–19] Reportedly, the sole edge increase with decreasing sheet area would cause such stability due to the improved ratio between hydrodynamic forces (electrostatic) and interlayer van der Waals forces;[18] however, not enough data are provided for supporting

[a] MackGraphe – Mackenzie Institute for Research in Graphene and Nanotechnologies, Mackenzie Presbyterian University, Rua da Consolação, 896, São Paulo, SP 01302-907, Brazil. E-mail: guilherminojmf@mackenzie.br

[b] Institute of Macromolecular Chemistry, Academy of Sciences of the Czech Republic, Heyrovsky Sq. 2, 162 06 Prague 6, Czech Republic. E-mail: donato@imc.cas.cz

† Electronic supplementary information (ESI) available. See DOI: 10.1039/c9cp06422b

Published on 11 December 2019. Downloaded by Universidade Presbiteriana Mackenzie on 12/20/2019 5:36:45 PM.

such a claim. Another hypothesis for explaining the stability of MoS_2 in H_2O is edge functionalization.[18] MoS_2 is known for promoting reactions such as hydrogen evolution reactions (HERs) and for presenting significantly increased catalytic activity at the edges.[20] This could lead to the introduction of edge-attached dangling bonds, which readily react with H_2O-forming functional groups (*e.g.*, –SH).[18]

Thus, taking into account both previously described hypotheses, herein we present a detailed experimental and theoretical investigation of the MoS_2 LPE, in search for elements that could help in explaining this anomalous stability of the exfoliated MoS_2 in H_2O medium.

Experimental

Materials

Molybdenum disulfide (MoS_2, 99%) with lateral size between 7 and 40 μm was obtained from Sigma Aldrich. Deionized H_2O was prepared using Milli-Q H_2O from the ALPAX Direct purification system. Acetone (AC) was acquired from Synth Company (P.A A.C.S. standard).

MoS_2 LPE process

Dispersions of 0.1 g of MoS_2 in 100 mL of solvent (H_2O or AC) were added in glass vials. The dispersions were exposed to different sonication times (30, 60, 120 and 180 minutes) using a bath ultrasound processor (Elma P30, 37 kHz at 30 ± 2 °C). Since the three shortest sonication times did not exhibit the expected degree of exfoliation (see ESI,† Fig. S1), all further characterization was performed for the sample after 180 minutes of sonication. After exfoliation, the dispersions were centrifuged for 60 minutes at 4000 rpm; then, the precipitated material was removed and the supernatant liquid was characterized.

Characterization

Scanning electron microscopy (SEM). For structural evaluation of MoS_2 crystals prior to the exfoliation process, they were deposited on the carbon tape substrate and characterized using an Olympus FEI 650 Scanning Electron Microscope (USA) at 2 kV. After exfoliation and centrifugation, the supernatant was vacuum filtered (pore size: 0.22 μm) on a nitrocellulose (water suspension) or nylon membrane (acetone suspension) and the retained material was analyzed or 1 μL of the supernatant liquid was deposited on a highly oriented pyrolytic graphite (HOPG) substrate. These materials were analyzed using a JEOL JSM-7800F microscope.

Atomic force microscopy (AFM). Aliquots of the supernatant after centrifugation were deposited on mica substrates following the drop casting method. The samples were left for a period of 24 hours in a desiccator for moisture evaporation and subsequently analyzed using a Bruker Icon Dimension microscope in ScanAsyst mode, with a ScanAsyst Air probe. The images were collected with 256 × 256 resolution points within an area of 50 × 50 μm.

Optical microscopy (OM). MoS_2 dispersions were placed on a Petri dish and analyzed under a Nikon optical microscope using a 20× objective lens.

Raman confocal spectroscopy. Aliquots of the supernatant after the process of exfoliation and centrifugation were deposited on an O-ring on a glass substrate and characterized by Raman spectroscopy utilizing a Witec model UHTS 300, using a green laser (532 nm).

UV-vis spectroscopy. The dispersions were placed in a quartz cuvette at room temperature and analyzed on Agilent Model 8453 single beam equipment. This technique was also used to evaluate the lateral size as well as the number of layers of the exfoliated material in H_2O with absorbance at 348 nm. The obtained absorbance value was utilized as a reference for MoS_2 particles.

Zeta potential (ZP) and dynamic light scattering (DLS). 700 μL of the supernatant was deposited on a DTS1070 folded capillary cuvette cell and analyzed in triplicate using a Malvern Instruments NANO ZS zetasizer. The nanoparticle size determination was performed by DLS with the same equipment, using 4 mL of the supernatant in polystyrene cuvettes with an optical path of 1 cm, using the standard equipment methodology for an aqueous medium at 25 °C.

Attenuated total reflection Fourier-transform infrared spectroscopy (ATR-FTIR). The characterization of MoS_2 in the bulk as well as the supernatant was performed using an IRTracer-100 (Shimadzu) infrared spectrometer in the range of 4000–1000 cm^{-1} and a resolution of 8 cm^{-1}. The dispersions were placed in a 1 mm thick KRS-5 Fixed Thickness Cell (P/N 202-32002-XX).

***Ab initio* quantum simulation based on density functional theory (DFT),[21,22] as implemented in the SIESTA code[23].** We used double-ζ basis with polarization orbitals (DZP), an energy shift of 0.03 eV, a mesh cutoff of 300 Ry, and norm-conserved pseudopotentials with Troullier–Martins parameterization.[24] The exchange–correlation functional was in generalized-gradient approximation with Perdew–Burke–Ernzerhof (PBE) parameterization.[25] The geometries were optimized with the criterion of forces smaller than 0.03 eV $Å^{-1}$.[26] For MoS_2 flakes, a spacing of approximately 15 Å was used between adjacent images to avoid spurious interaction with periodic images. Partial charges were calculated using the Voronoi deformation density method.[27] Electrostatic maps were calculated with electronic density isosurfaces colored with Hartree potential values. Blue regions in electrostatic maps represent positive net charges, red regions represent negative net charges, and green regions represent charge neutrality. Volumetric data analysis was made using the VESTA program.[28]

Results and discussion

The LPE media used in this work were H_2O and acetone (Ac), where the latter is an extensively used reference medium.[17–19]

This journal is © the Owner Societies 2019

Published on 11 December 2019. Downloaded by Universidade Presbiteriana Mackenzie on 12/20/2019 5:36:45 PM.

The nanomaterial dispersions within these liquid media were partially predicted by the Hansen solubility theory that follows the equation:

$$R_a = \sqrt{4(\delta_{D1} - \delta_{D2})^2 + (\delta_{P1} - \delta_{P2})^2 + (\delta_{H1} - \delta_{H2})^2} \quad (1)$$

and considers three parameters: (i) dispersive (δ_D) and (ii) polar (δ_P) components, and (iii) hydrogen interactions (δ_H),[15] indicating that the smaller the R_a the better the solubility.[29] Thus, Ac should present better solvent character for MoS_2 (R_a = 5.19) than H_2O (R_a = 35.67), indicating a stronger interaction between particles and liquid. However, after exfoliation and centrifugation the opposite was observed. The MoS_2 LPE in H_2O medium produced a very stable supernatant, with negligible material deposition and long-term dispersion stability (months). In contrast, MoS_2 LPE in Ac presented precipitates within only three days (Fig. 1a). These observations are in agreement with other reports.[17–19] The layered structure of the pristine MoS_2 observed in SEM images (Fig. 1b and c) was destroyed after LPE in Ac (Fig. 1d) while it maintained its structural integrity after LPE in H_2O medium (Fig. 1e). Additionally, MoS_2 LPE in Ac presented more bulky aggregates with apparent crystal edge damage (see ESI,† Fig. S2–S4). These defects were most likely introduced by the ultrasonic exfoliation process that is governed by cavitation mechanisms, in which the viscosity of the medium plays an important role in the exfoliation process. The viscosity of water at 25 °C is 1 cP, while that of acetone is 0.3 cP.[30,31] In addition to viscosity, solvent volatility also plays an important role in cavitation processes as it limits the size of the bubble formed and, consequently, affects the amount of energy released during cavitation, giving water an advantage in the cavitation process. These results were also confirmed by AFM, where MoS_2 crystals obtained by LPE in H_2O display much thinner and well dispersed sheets (Fig. 2a and b), in comparison to those obtained in Ac medium (Fig. 2c and d). For a reliable comparison between the systems, the topological screenings of the exfoliated materials (extracted from AFM data) were presented as histograms, considering the platelets' lateral size (Fig. 2e) and thickness distribution (Fig. 2f). According to the platelets' thickness distribution histogram, MoS_2 LPE in H_2O produces majority of crystals with thickness below 6 nm. Considering the

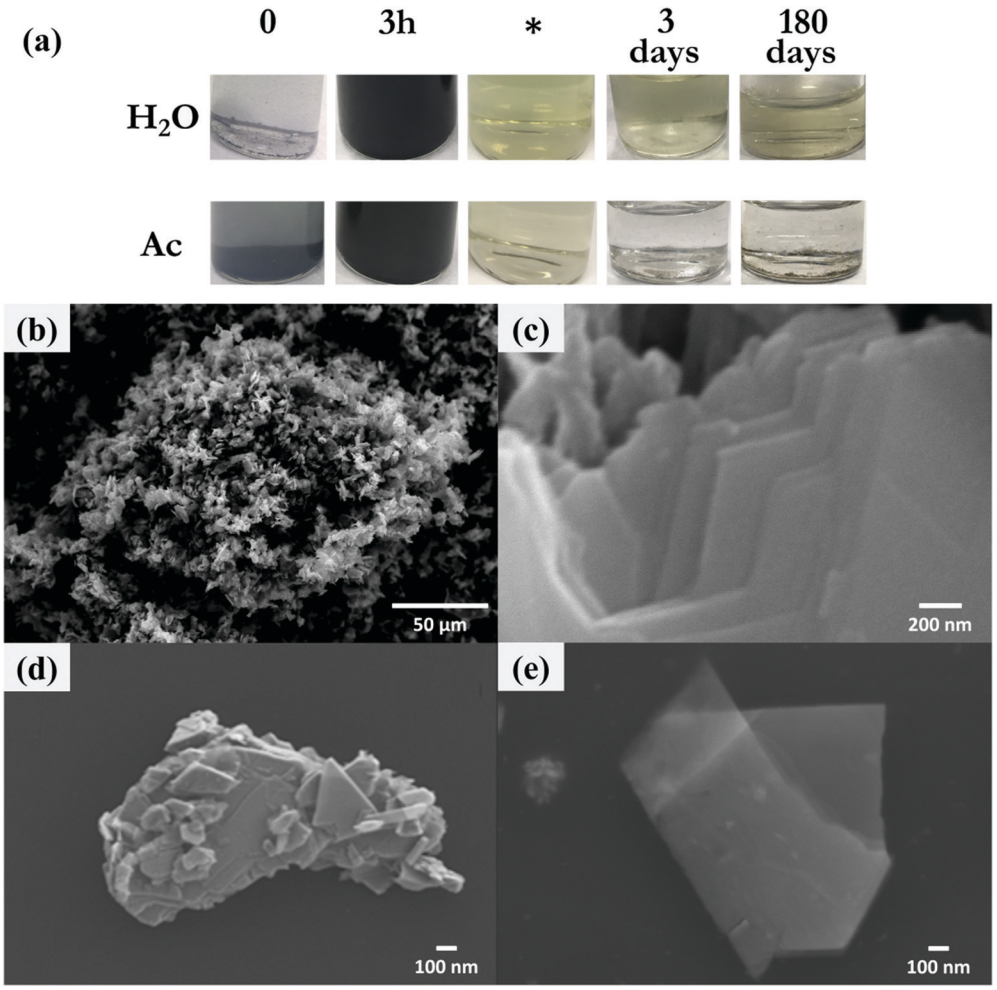

Fig. 1 (a) Images of MoS_2 dispersion in H_2O and Ac at different timeframes, where * indicates the centrifuged sample. SEM images of the pristine (bulk) MoS_2 under different magnifications (b and c) as well as MoS_2 nanosheets after LPE in Ac (d) and H_2O (e).

Published on 11 December 2019. Downloaded by Universidade Presbiteriana Mackenzie on 12/20/2019 5:36:45 PM.

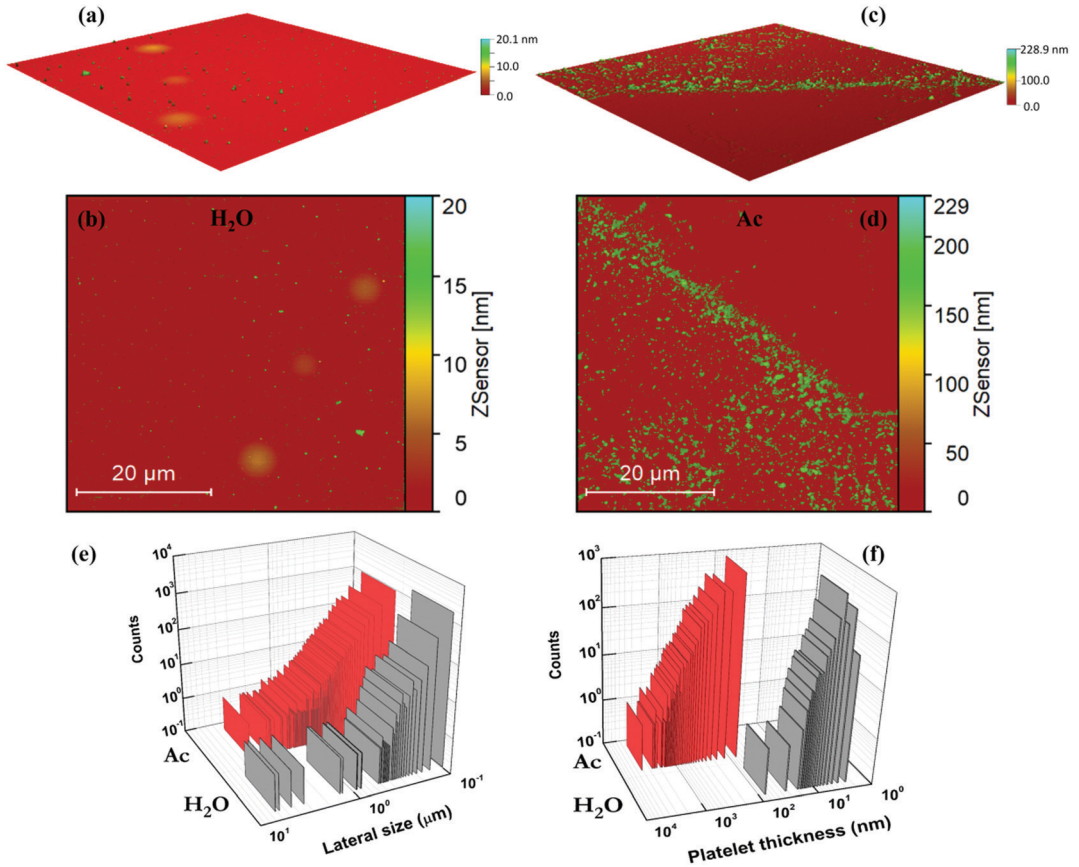

Fig. 2 3D and 2D AFM maps of MoS_2 particles' height distribution (green) in H_2O (a and b) and Ac (c and d); AFM histograms of platelets' lateral size (e) and thickness (f) after LPE in H_2O and Ac, respectively.

first layer with 1 nm and the subsequent ones with approximately 0.7 nm,[32,33] most of the crystals presented less than 7 layers. These crystals were smaller presenting an average lateral size of 133 nm (diagonal dimension of 188 nm). For LPE in Ac, the exfoliation process was much less effective producing larger crystals with an average lateral size of 241 nm (diagonal dimension of 340 nm) and a minimum thickness of least 60 nm, which corresponds to more than 80 layers. Very recently, much more stable MoS_2 dispersions in Ac, presenting much less sheet layers, were reported.[34] Interestingly, the authors also report MoS_2 edge functionalization, however, only under more intense sonication conditions producing molybdenum oxide edges *via* sonochemical oxidation reaction. In our system, these conditions were not reached, thus not producing such stable MoS_2 dispersions in Ac. Despite different conditions, interestingly, they obtained similar lateral size of the stable MoS_2 sheets (<200 nm). Since the edge perimeter inversely increases with lateral size, this lateral size range seems to be the threshold for the edge-functionalization contribution to start being significant, affecting the sheet stabilization within the solvent.

The particle size of MoS_2 LPE in H_2O was also evaluated by DLS (considering their hydrodynamic radius) where most of the platelet sizes were ranging from 30 to 200 nm (Fig. 3a), also in agreement with the AFM results. Thus, regarding structural integrity, dispersion stabilization and number of layers after the exfoliation process, we opted to focus the exfoliation study only when H_2O was used. Raman spectroscopy was used for estimating the average number of MoS_2 layers when exfoliated in H_2O. Considering polytype layered 2H-MoS_2, four active vibrational modes are present (E^2_{2g}, E_{1g}, E^1_{2g} and A^1_{2g}) and these absorption bands correspond to four electronic transition types (A, B, C and D).[13] It is known that the distance between the in-plane S atom (E^1_{2g}) and out-of-plane S atom (A_{1g}) vibrational modes corresponds to the crystal thickness and as consequence it can be used as a parameter to evaluate the exfoliation degree.[35] Thus, the degree of MoS_2 exfoliation was measured by the distance between the $E^1_{2g} = 383\ cm^{-1}$ and $A_{1g} = 408\ cm^{-1}$ vibrational modes[36] (Fig. 3b), where several spectra were collected (30 in average) to obtain a statistical distribution (Fig. 3c). A defined decrease of spacing between the vibrational modes E_{2g} and A_{1g} is observed for different samples after the LPE process, varying between 24 and 26.5 cm^{-1}, representing ≤ 5 layers.[37] These results are in agreement with the AFM experimental data (Fig. 2), showing an effective MoS_2 LPE in H_2O.

To estimate the residual stable concentration after centrifugation, the MoS_2 dispersion in H_2O was characterized by UV/vis spectrometry.[38,39]

The concentration of MoS_2 was determined by the Lambert Beer Law, where the absorbance divided by cell length at set

This journal is © the Owner Societies 2019

Published on 11 December 2019. Downloaded by Universidade Presbiteriana Mackenzie on 12/20/2019 5:36:45 PM.

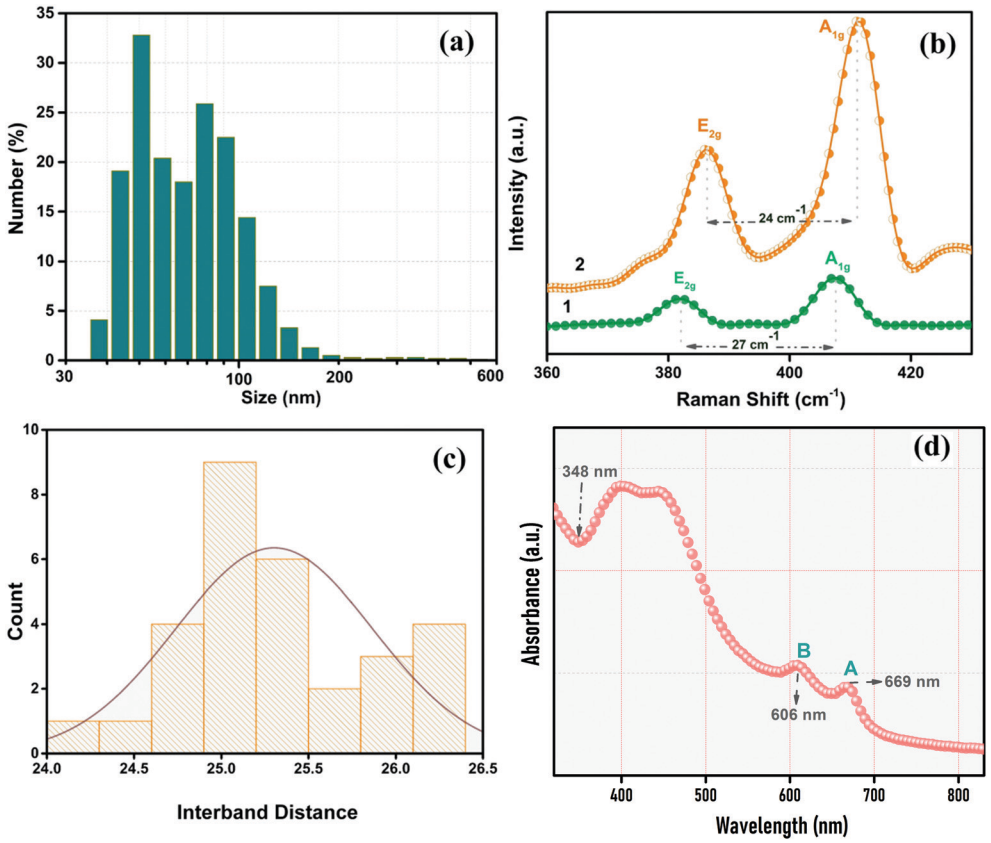

Fig. 3 (a) The particle size distribution of the H_2O dispersion after LPE, obtained by DLS; (b) Raman spectra before (curve 1) and after (curve 2) LPE in H_2O; (c) a histogram showing the Gaussian distribution curve of the distance between E_{2g} and A_{1g}; (d) UV/vis spectrum of dispersion in H_2O, after LPE and centrifugation.

wavelength was used as a semiquantitative measure of dispersibility $\left(\frac{A}{l} = \alpha c\right)$.[15] When considering α_{669} = 238 L g^{-1} m^{-1} and $\frac{A}{l} \cong 4.3$ for λ = 669 nm, the estimated concentration was 0.018 mg mL^{-1}. Thus, for the initial MoS_2 concentration of 1 mg mL^{-1} the exfoliation efficiency in H_2O was 18%. In this way, the measured absorbance (λ = 672 nm) of the dispersion was 0.037, and the concentration was calculated as 0.0142 mg mL^{-1}. Moreover, absorbance peaks located at 668 nm and 609 nm (Fig. 3d) were used as references for determining the particle size (eqn (2)) and the number of MoS_2 layers (eqn (3))

$$L\,(\mu\text{m}) = \frac{3.5\dfrac{\text{Ext}_b}{\text{Ext}_{348}} - 0.14}{11.5 - \dfrac{\text{Ext}_b}{\text{Ext}_{348}}}. \quad (2)$$

$$N = 2.3 \times 10^{36} e^{-54\,888/\lambda_A} \quad (3)$$

where Ext_b is the absorbance at peak b in the UV/vis spectrum and Ext_{348} is the absorbance at 348 nm, with a margin of error $\leq$10%.[40] Thus, the calculated particle lateral size (L) was 140 nm, while the number of layers was estimated as $\leq$5, perfectly correlating with both AFM and Raman characterization and confirming the high degree of exfoliation obtained. Interestingly, although the surface energy of MoS_2 is 46.5 mJ m^{-2},[3] and H_2O presents too high surface tension (72.75 mJ m^{-2})[14] to be a good solvent for the MoS_2 LPE process, the results displayed an opposite behavior indicating that interfacial energy is not the ruling parameter for obtaining well-dispersed and stable 2D materials. The MoS_2 dispersion stability in H_2O, after centrifugation, was further investigated by zeta potential. This investigation is an important factor in characterizing the stability of colloidal dispersions as it provides a measure of effective surface charge associated with the double layer around the colloidal particle. It is known that particles with zeta potentials $>$+30 mV or $<$−30 mV have stable dispersions due to electrostatic repulsion between particles.[18,19] Thus, the obtained results (−32.1 mV) indicate good stability, contradicting the values predicted by Hansen's law and indicating a process-based modification in the exfoliated MoS_2.

As previously discussed, the increased MoS_2 stability in water, with decreasing sheet size, is an already described phenomenon.[18] However, besides the increase of the edge perimeter, no plausible explanation for this phenomenon has been given. Considering the hypothesis that edge modification would cause such an anomalous stability of the exfoliated MoS_2 in H_2O, one can consider an increase in anisotropy at the platelets. For this reason, a MoS_2/H_2O dispersion was left in an open flask for slow solvent evaporation and concentration

Published on 11 December 2019. Downloaded by Universidade Presbiteriana Mackenzie on 12/20/2019 5:36:45 PM.

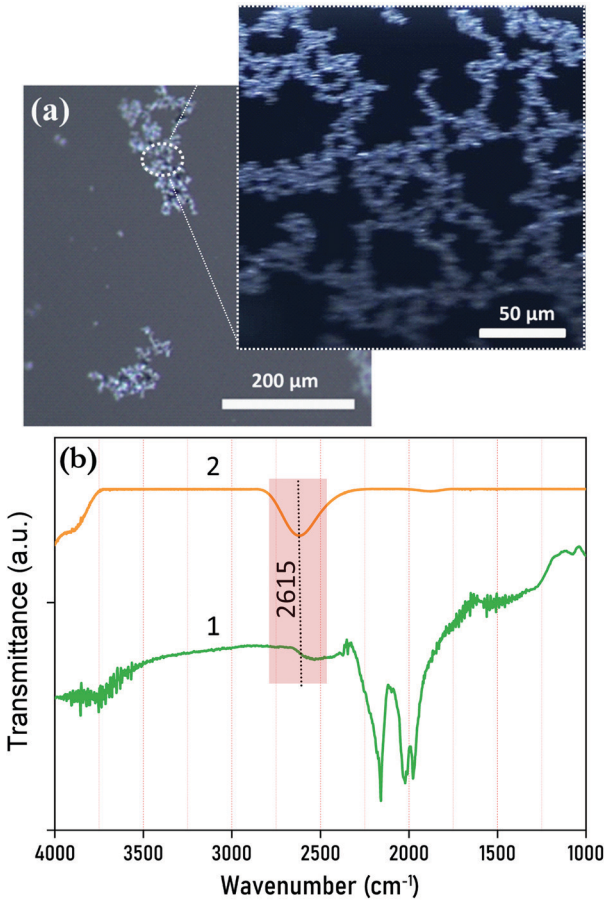

Fig. 4 (a) OM micrographs of LPE MoS_2 after self-assembly by partial solvent evaporation under different magnifications; (b) ATR-FTIR spectra of MoS_2 in the bulk (1) and after LPE in H_2O (2).

increase, decreasing the dispersion stability. Interestingly, with the increase in concentration, fiber-like agglomerations started to form. When this agglomerated material was characterized by OM, the formation of a physical network could be observed, where the MoS_2 platelets seem to assemble side-by-side (Fig. 4a). A very similar effect was observed elsewhere, but for edge modified graphene oxide after controlled deposition.[41] On the other hand, this effect could not be observed for MoS_2 LPE in Ac, reassuring the suspicion of a MoS_2 edge modification caused by the exfoliation medium (H_2O) amplified by the intense cavitation energy. As previously mentioned, MoS_2 edge functionalization using Ac as solvent under more intense sonication conditions was recently reported,[34] producing molybdenum oxide edges *via* sonochemical oxidation reaction, which suggests that the functionalization using H_2O may be reached in milder conditions and with a more environmental friendly solvent. Previous studies have already suggested that MoS_2 edge S atoms could be functionalized during a H_2O cleavage process (–SH) or react with both H_2O and dissolved O_2 during the intense cavitation ($-HSO_3$).[18] However, to our knowledge, the discussion concerning this edge effect on platelet stabilization is almost negligible. More information is necessary to understand if only the catalytic sites are enough to stabilize MoS_2 in H_2O or this stability is achieved only after the edge functionalization.

Thus, to evidence S–H functionalization at the MoS_2 edges after the exfoliation, ATR-FTIR spectra were collected. ATR-FTIR spectra of MoS_2 in the bulk and after LPE in H_2O were obtained in the range 1000–4000 cm^{-1} (Fig. 4b). After exfoliation, characteristic peaks in the range 2000–2250 cm^{-1} for MoS_2 in the bulk disappeared and a wide band (2400–2800 cm^{-1}) centered at 2615 cm^{-1} could be observed. According to the literature, the thiol band (–SH) should appear at 2540 cm^{-1} or 2563 cm^{-1}.[42,43] This result corroborates the aforementioned hypothesis of a change in the chemical structure of MoS_2, and suggests that this change was associated to –SH group formation.

Consequently, using *ab initio* quantum simulations, we evaluated the effect of MoS_2 edge functionalization (S atom functionalization during the H_2O cleavage process forming 2H-MoS_2), and compared to the pristine MoS_2 crystals (Fig. 5). Therefore, we simulated two triangular flakes with approximately 13 Å side length. The first flake has the optimized geometry without adsorption of H at the edges (bare-edge), while the second one has the geometry optimized with H adsorption, forming –SH groups at the edges (thiol-edge). Firstly, we noticed that the thiol-edge optimized geometry kept the crystallinity of MoS_2 higher than the bare-edge. The optimized geometries are shown in Fig. 5a. The H stability at the edges was evaluated through Gibbs free energy for H adsorption, given by

$$\Delta G_H(T,p) = \frac{1}{n_H}[E(\text{thiol-edge}) - E(\text{bare-edge})] - \mu_H(T,p) \quad (4)$$

where n_H = 24 is the number of H atoms in thiol-edge flakes, E(thiol-edge) is the total energy of thiol-edge flakes, E(bare-edge) is the total energy of bare-edge flakes, and $\mu_H(T,p)$ is the chemical potential for H depending on temperature T and pressure p.

This chemical potential varies according to the source of H. In our case, we calculated the chemical potential coming from both molecular hydrogen (H_2) and H_2O (H_2O/O_2). Using *ab initio* methods based on DFT we calculated the Gibbs free energy in the absence of temperature and pressure effects. In this case, we obtained $\Delta G_H^{H_2} = -27.3$ kJ mol^{-1} and $\Delta G_H^{H_2O/O_2} = +92.4$ kJ mol^{-1}. Variations of the chemical potential with temperature and pressure could be modeled according to an ideal gas:[44,45]

$$\mu_H^{H_2}(T,p) = \mu_H^{H_2} + \frac{\Delta G_{H_2}(T,p_0)}{2} + RT\log\left(\frac{p}{p_0}\right) \quad (5)$$

for H from the H_2 source, and

$$\mu_H^{H_2O/O_2}(T,p) = \mu_H^{H_2O/O_2} + \frac{2\Delta G_{H_2O}(T,p_0) - \Delta G_{O_2}(T,p_0)}{4} + RT\log\left(\frac{p}{p_0}\right) \quad (6)$$

for H from the H_2O/O_2 source. In these equations, p_0 = 1 bar is the standard state pressure and R is the gas constant.

This journal is © the Owner Societies 2019

Published on 11 December 2019. Downloaded by Universidade Presbiteriana Mackenzie on 12/20/2019 5:36:45 PM.

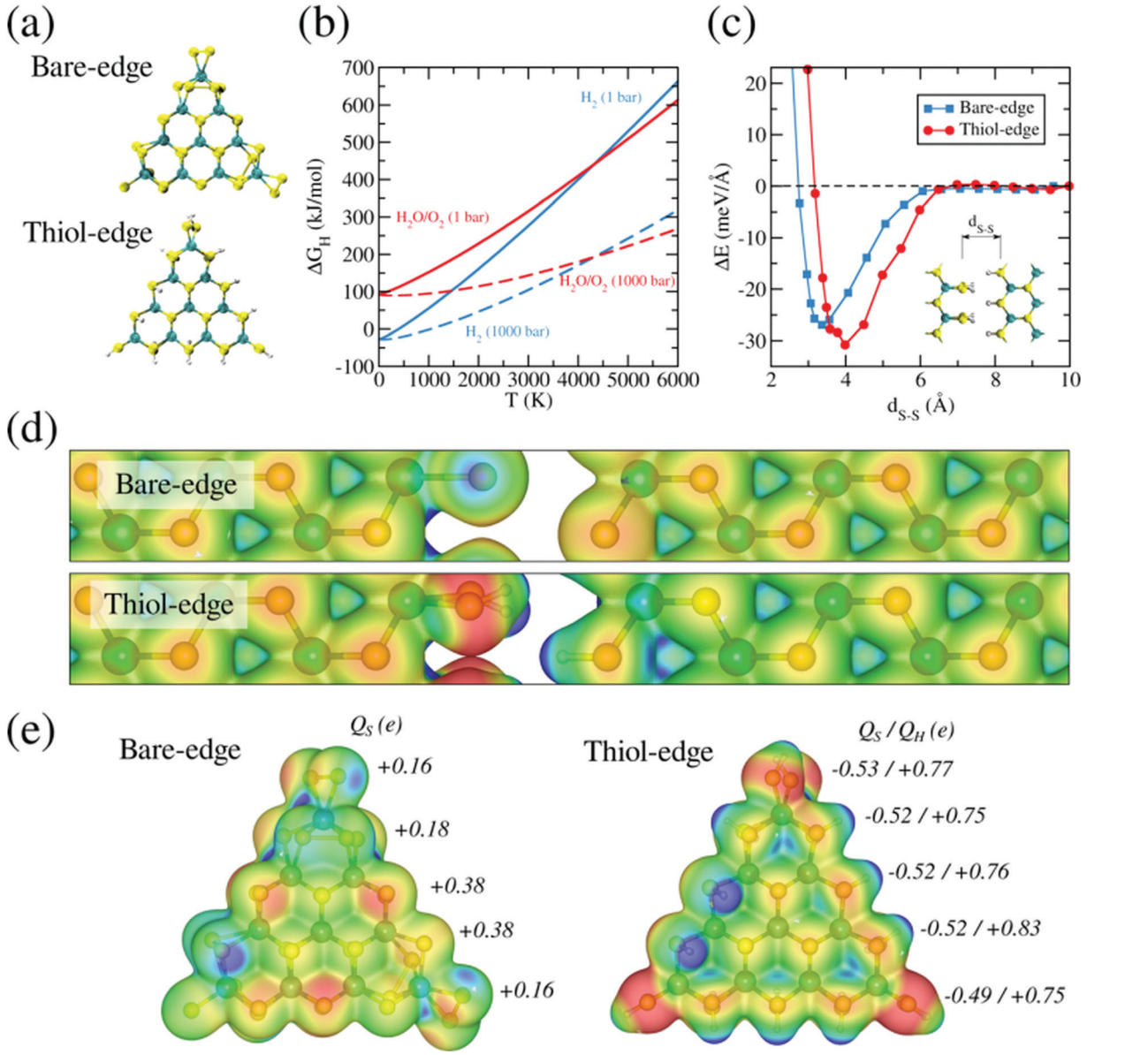

Fig. 5 *Ab initio* quantum simulation showing the ball-and-stick model for MoS_2 flakes without (bare-edge) and with H passivation (thiol-edge) (a); Gibbs free energy for H adsorption as a function of temperature, pressure and H source (b); edge–edge interaction energy as a function of the distance between two bare-edges and two thiol-edges (c); electrostatic map for bare-edge and thiol-edge close to energy minimum with distance (d); electrostatic map for MoS_2 flakes, and partial charges for S and H atoms of one side of the flake (e).

Combining the *ab initio* calculations for $\mu_H^{H_2}$ and $\mu_H^{H_2O/O_2}$, and the NIST-JANAF thermochemical tables,[46] we obtained the Gibbs free energies shown in Fig. 5b. For temperature $T = 4300$ K, the energy $\Delta G_H^{H_2O/O_2}$ was smaller than $\Delta G_H^{H_2}$, making it more favorable for H_2O to serve as the H source. At high pressures, the Gibbs free energies were smaller, but the transition was maintained at $T = 4300$ K. Coincidently, those are the very conditions produced during the sonication process, which easily reach 5000 K and 500 atm at the cavitation hot-spot.[47] This suggests that, besides the exfoliation by microstreaming, microjets, and shock waves (sonophysical process),[48] MoS_2 also suffers a sonochemical edge modification in the presence of H_2O, which is self-catalyzed and the ideal conditions are induced by the cavitation process. To understand the effects caused by this functionalization, the interaction between MoS_2 edges was obtained from total energy variations with the distance of S (d_{S-S}), shown in the inset of Fig. 5c. The potential energy between two bare-edges and that between two thiol-edges are also shown in Fig. 5c. A stronger interaction was observed between thiol-edges, in comparison to bare-edges. This intensification could be explained by the formation of electric dipoles in the thiol functional groups, shown qualitatively on electrostatic maps (Fig. 5d and e). Moreover, quantitative analysis, through the partial charges of S and H for one side of MoS_2 flakes, is shown in Fig. 5e. Interestingly, the MoS_2 edge regions with the most intense dipole formation are

Published on 11 December 2019. Downloaded by Universidade Presbiteriana Mackenzie on 12/20/2019 5:36:45 PM.

strongly associated with the functionalized edge, as recently demonstrated both by simulation[49] and experimentally.[20] Due to the high mobility, the edge thiol group is oriented in a way that minimizes the energy of the dipole–dipole interaction, resulting in edge–edge interaction intensification.

Conclusions

In summary, we experimentally demonstrated that H_2O acts as an efficient medium for the ultrasound-based liquid-phase exfoliation of MoS_2, forming a very stable dispersion of few-layer MoS_2, contradicting the Hansen theory for dispersion stability. This contradiction occurred because the effectiveness of the exfoliation process was dependent not only on the MoS_2 surface energy but also on a modification process that happened at the edges, changing completely the MoS_2 dispersion behavior. Moreover, *ab initio* quantum simulations allowed us to evaluate the effect of exfoliation conditions on the edge modification, indicating that the exfoliation conditions under sonication (high local pressure and temperature) provide a dual sonophysical/sonochemical process, both exfoliating and functionalizing the edges of MoS_2 with H atoms provided by H_2O molecules. Consequently, this edge-functionalization with H atoms caused both the anomalous stability of exfoliated MoS_2 sheets in H_2O medium and an edge–edge assembly, led by dipole interactions observed during MoS_2 re-agglomeration forced by solvent evaporation.

Conflicts of interest

There are no conflicts to declare.

Acknowledgements

The authors acknowledge FAPESP (Grants 2012/50259-8, 2017/00486-1 and 2018/10910-8), CAPES, and CNPq/Brazil (Grant 306422/2017-4) for financial support. This study was also supported in part by the Coordenação de Aperfeiçoamento de Pessoal de Nível Superior – Brasil (CAPES) – PRINT 88887.310339/2018-00. This work has also received funding from the European Union's Horizon2020-MSCARISE-734164 Graphene 3D Project, and MackPesquisa (Project number 181009). KZD and RKD acknowledge the financial support of the Ministry of Education, Youth and Sports of CR (project POLYMAT LO1507). LS is thankful for the high-performance computational facilities from Sdumont/LNCC supercomputer.

References

1 K. S. Novoselov, A. K. Geim, S. V. Morozov, D. Jiang, Y. Zhang, S. V. Dubonos, I. V. Grigorieva and A. A. Firsov, *Science*, 2004, **306**, 666–669.
2 J. N. Coleman, M. Lotya, A. O'Neill, S. D. Bergin, P. J. King, U. Khan, K. Young, A. Gaucher, S. De, R. J. Smith, I. V. Shvets, S. K. Arora, G. Stanton, H.-Y. Kim, K. Lee, G. Tae Kim, G. S. Duesberg, T. Hallam, J. J. Boland, J. J. Wang, J. F. Donegan, J. C. Grunlan, G. Moriarty, A. Shmeliov, R. J. Nicholls, J. M. Perkins, E. M. Grieveson, K. Theuwissen, D. W. McComb, P. D. Nellist and V. Nicolosi, *Science*, 2011, **331**, 568–571.
3 A. Jawaid, D. Nepal, K. Park, M. Jespersen, A. Qualley, P. Mirau, L. F. Drummy and R. A. Vaia, *Chem. Mater.*, 2016, **28**, 337–348.
4 Q. H. Wang, K. Kalantar-Zadeh, A. Kis, J. N. Coleman and M. S. Strano, *Nat. Nanotechnol.*, 2012, **7**, 699–712.
5 L. Niu, J. N. Coleman, H. Zhang, H. Shin, M. Chhowalla and Z. Zheng, *Small*, 2016, **12**, 272–293.
6 M. Acerce, D. Voiry and M. Chhowalla, *Nat. Nanotechnol.*, 2015, **10**, 313.
7 V. Nicolosi, M. Chhowalla, M. G. Kanatzidis, M. S. Strano and J. N. Coleman, *Science*, 2013, **340**, 1226419.
8 C. Rao, U. Maitra and U. V. Waghmare, *Chem. Phys. Lett.*, 2014, **609**, 172–183.
9 K. F. Mak, C. Lee, J. Hone, J. Shan and T. F. Heinz, *Phys. Rev. Lett.*, 2010, **105**, 136805.
10 G. Eda, H. Yamaguchi, D. Voiry, T. Fujita, M. Chen and M. Chhowalla, *Nano Lett.*, 2011, **11**, 5111–5116.
11 K. P. Dhakal, D. L. Duong, J. Lee, H. Nam, M. Kim, M. Kan, Y. H. Lee and J. Kim, *Nanoscale*, 2014, **6**, 13028–13035.
12 H.-X. Zhang, X.-Q. Zhang and K.-B. Yoon, *Polymers*, 2017, **9**, 490.
13 H. Li, Q. Zhang, C. C. R. Yap, B. K. Tay, T. H. T. Edwin, A. Olivier and D. Baillargeat, *Adv. Funct. Mater.*, 2012, **22**, 1385–1390.
14 A. Ciesielski and P. Samorì, *Chem. Soc. Rev.*, 2014, **43**, 381–398.
15 J. Shen, Y. He, J. Wu, C. Gao, K. Keyshar, X. Zhang, Y. Yang, M. Ye, R. Vajtai, J. Lou and P. M. Ajayan, *Nano Lett.*, 2015, **15**, 5449–5454.
16 G. Levita, P. Restuccia and M. C. Righi, *Carbon*, 2016, **107**, 878–884.
17 V. Forsberg, R. Zhang, J. Bäckström, C. Dahlström, B. Andres, M. Norgren, M. Andersson, M. Hummelgård and H. Olin, *PLoS One*, 2016, **11**, e0154522.
18 H. Ma, Z. Shen and S. Ben, *J. Colloid Interface Sci.*, 2018, **517**, 204–212.
19 J. Kim, S. Kwon, D.-H. Cho, B. Kang, H. Kwon, Y. Kim, S. O. Park, G. Y. Jung, E. Shin, W.-G. Kim, H. Lee, G. H. Ryu, M. Choi, T. H. Kim, J. Oh, S. Park, S. K. Kwak, S. W. Yoon, D. Byun, Z. Lee and C. Lee, *Nat. Commun.*, 2015, **6**, 8294.
20 A. Parija, Y.-H. Choi, Z. Liu, J. L. Andrews, L. R. De Jesus, S. C. Fakra, M. Al-Hashimi, J. D. Batteas, D. Prendergast and S. Banerjee, *ACS Cent. Sci.*, 2018, **4**, 493–503.
21 P. Hohenberg and W. Kohn, *Phys. Rev.*, 1964, **136**, B864.
22 W. Kohn and L. J. Sham, *Phys. Rev.*, 1965, **140**, A1133.3.
23 J. M. Soler, E. Artacho, J. D. Gale, A. García, J. Junquera, P. Ordejón and D. Sánchez-Portal, *J. Phys.: Condens. Matter*, 2002, **14**, 2745.
24 N. Troullier and J. L. Martins, *Phys. Rev. B: Condens. Matter Mater. Phys.*, 1991, **43**, 1993.
25 J. P. Perdew, K. Burke and M. Ernzerhof, *Phys. Rev. Lett.*, 1996, 77, 3865.

Published on 11 December 2019. Downloaded by Universidade Presbiteriana Mackenzie on 12/20/2019 5:36:45 PM.

26 R. P. Feynman, *Phys. Rev.*, 1939, **56**, 340.
27 C. Fonseca Guerra, J. W. Handgraaf, E. J. Baerends and F. M. Bickelhaupt, *J. Comput. Chem.*, 2004, **25**, 189–210.
28 K. Momma and F. Izumi, *J. Appl. Crystallogr.*, 2011, **44**, 1272–1276.
29 M. Yi, Z. Shen, X. Zhang and S. Ma, *J. Phys. D: Appl. Phys.*, 2012, **46**, 025301.
30 J. A. Åström, F. Ouchterlony, R. Linna and J. Timonen, *Phys. Rev. Lett.*, 2004, **92**, 245506.
31 A. Liscio, K. Kouroupis-Agalou, X. D. Betriu, A. Kovtun, E. Treossi, N. M. Pugno, G. De Luca, L. Giorgini and V. Palermo, *2D Mater.*, 2017, **4**, 025017.
32 M. Zhang, R. C. T. Howe, R. I. Woodward, E. J. R. Kelleher, F. Torrisi, G. Hu, S. V. Popov, J. R. Taylor and T. Hasan, *Nano Res.*, 2015, **8**, 1522–1534.
33 P. Nemes-Incze, Z. Osváth, K. Kamarás and L. Biró, *Carbon*, 2008, **46**, 1435–1442.
34 A. A. Graf, M. J. Large, S. P. Ogilvie, Y. Rong, P. J. Lynch, G. Fratta, S. Ray, A. Shmeliov, V. Nicolosi, R. Arenal, A. A. K. King and A. B. Dalton, *Nanoscale*, 2019, **11**, 15550–15560.
35 C. Lee, H. Yan, L. E. Brus, T. F. Heinz, J. Hone and S. Ryu, *ACS Nano*, 2010, **4**, 2695–2700.
36 H. Zhang, S. B. Lu, J. Zheng, J. Du, S. C. Wen, D. Y. Tang and K. P. Loh, *Opt. Express*, 2014, **22**, 7249–7260.
37 L. Liang and V. Meunier, *Nanoscale*, 2014, **6**, 5394–5401.
38 C. Backes, T. M. Higgins, A. Kelly, C. Boland, A. Harvey, D. Hanlon and J. N. Coleman, *Chem. Mater.*, 2016, **29**, 243–255.
39 X. Fan, P. Xu, Y. C. Li, D. Zhou, Y. Sun, M. A. T. Nguyen, M. Terrones and T. E. Mallouk, *J. Am. Chem. Soc.*, 2016, **138**, 5143–5149.
40 C. Backes, R. J. Smith, N. McEvoy, N. C. Berner, D. McCloskey, H. C. Nerl, A. O'Neill, P. J. King, T. Higgins, D. Hanlon, N. Scheuschner, J. Maultzsch, L. Houben, G. S. Duesberg, J. F. Donegan, V. Nicolosi and J. N. Coleman, *Nat. Commun.*, 2014, **5**, 4576.
41 K. Gleason, S. Saraf, S. Seal and S. A. Putnam, *ACS Omega*, 2018, **3**, 1154–1158.
42 J. S. Kim, H. W. Yoo, H. O. Choi and H. T. Jung, *Nano Lett.*, 2014, **14**, 5941–5947.
43 S. S. Chou, M. De, J. Kim, S. Byun, C. Dykstra, J. Yu, J. Huang and V. P. Dravid, *J. Am. Chem. Soc.*, 2013, **135**, 4584–4587.
44 K. Reuter and M. Scheffler, *Phys. Rev. B: Condens. Matter Mater. Phys.*, 2001, **65**, 035406.
45 M. Bollinger, K. W. Jacobsen and J. K. Nørskov, *Phys. Rev. B: Condens. Matter Mater. Phys.*, 2003, **67**, 085410.
46 M. W. Chase Jr, *NIST-JANAF Thermochemical Tables*, American Institute of Physics, 4th edn, 1998.
47 K. S. Suslick, *Science*, 1990, **247**, 1439–1445.
48 S. K. Sharma, D. Chen and A. Mudhoo, *Handbook on applications of ultrasound: sonochemistry for sustainability*, CRC Press, 2011.
49 G. Li, D. Zhang, Q. Qiao, Y. Yu, D. Peterson, A. Zafar, R. Kumar, S. Curtarolo, F. Hunte, S. Shannon, Y. Zhu, W. Yang and L. Cao, *J. Am. Chem. Soc.*, 2016, **138**, 16632–16638.